PAPER

Check for updates

Abnormal anti-thermal quenching of Mn^{2+} and reverse thermal response of Mn^{2+}/Mn^{4+} luminescence in garnet phosphor for wide-range temperature sensing†

Annu Balhara,[ab] Santosh K. Gupta, [iD] *[ab] G. D. Patra, [iD] [c] Boddu S. Naidu [iD] [d] and Kathi Sudarshan [iD] [ab]

Herein, we explored the diverse temperature-dependent luminescence, thermal quenching, and decay kinetics of Mn^{2+}/Mn^{4+} emission centers in a Y$_3$Al$_2$Ga$_3$O$_{12}$ garnet host. Emission color tuning was achieved from red to deep red region as a function of the Mn doping amount. The tuning of the Mn valence state as a function of doping concentration in Y$_3$Al$_2$Ga$_3$O$_{12}$ was investigated in detail, and the mechanism of self-reduction of Mn^{4+} has been discussed. Interestingly, the temperature-dependent photoluminescence study of Y$_3$Al$_2$Ga$_3$O$_{12}$:Mn$^{2+/4+}$ revealed the abnormal anti-thermal quenching of the Mn^{2+} emission band with increasing temperature. In contrast, Mn^{4+} emission displayed thermal quenching with increase in temperature. The interplay of self-reduction and defects in the anti-thermal quenching of Mn^{2+} has been discussed. Benefiting from the reverse temperature-dependent luminescence behaviour of Mn$^{2+/4+}$, luminescence ratiometric and lifetime thermometry have demonstrated a promising wide temperature sensing range, from cryogenic conditions (10 K) to 490 K. A high relative sensitivity of 2.35% K^{-1} (190 K) and 3.10% K^{-1} (390 K) could be achieved for ratiometric and lifetime thermometry, respectively. The lifetime thermometer based on the lifetime of Mn^{2+} and Mn^{4+} ions offered good temperature resolution (<0.30 K). This work proposed the use of dual-emitting single-doped materials for highly sensitive wide sensing range thermometry and offers meaningful advancement in the design of orange–red emitting phosphors.

1. Introduction

Phosphor materials have emerged as potential sources of solid-state lighting technology for indoor/outdoor illumination, displays, optoelectronics, and light-emitting diodes (LEDs) applications.[1–6] The transition metal manganese (Mn$^{2+/4+}$ ions) is a well-known photoluminescence activator for various inorganic luminescent materials used in modern lighting sources owing to red emission with high luminous efficiency, low cost and non-rare earth-based red phosphors.[7–11] Mn^{2+}-based phosphors have been widely investigated to achieve multimode fluorescence for the design of white LEDs, thermal sensing, and anti-counterfeiting applications.[12,13] Garnet phosphors (A$_3$B$_2$C$_3$O$_{12}$) are popular candidates for achieving

the strong red to deep red emission of Mn$^{2+/4+}$ ions as they can be stabilized in octahedral Al^{3+}/Ga^{3+} sites.[14,15] The high temperature solid-state synthesis of the garnet structure may result in the coexistence of Mn$^{2+/4+}$ ions due to the defect-induced self-reduction of Mn^{4+} ions. The design of Mn$^{2+/4+}$-activated materials offers the potential optimization of emission from red light (Mn^{2+}) to deep red light (Mn^{4+}) by controlling the composition and tuning the emission for indoor plant growth. Since the control of the Mn valence state is a great challenge for developing Mn-activated luminescent materials, few studies have reported dual-emitting Mn$^{2+/4+}$ phosphors for suitable applications.[14–20] Therefore, understanding the photophysical properties, defect-induced self-reduction, charge transfer dynamics, decay kinetics and thermal behaviour is essential for designing Mn-based phosphors for targeted applications utilizing the multiple valence states of Mn. The mixed valence of Mn offers the development of multifunctional phosphors with emission tunability, which is promising for the development of phosphors for indoor plant lighting, anti-counterfeiting, optoelectronics and temperature sensing applications.

[a] *Radiochemistry Division, Bhabha Atomic Research Centre, Trombay, Mumbai-400085, India. E-mail: santoshg@barc.gov.in, santufrnd@gmail.com*

[b] *Homi Bhabha National Institute, Anushaktinagar, Mumbai-400094, India*

[c] *Technical Physics Division, Bhabha Atomic Research Centre, Trombay, Mumbai-400085, India*

[d] *Institute of Nano Science and Technology, Mohali-140306, India*

† Electronic supplementary information (ESI) available. See DOI: https://doi.org/10.1039/d4tc03650f

This journal is © The Royal Society of Chemistry 2024

J. Mater. Chem. C, 2024, **12**, 19671–19680 | **19671**

Benefitting from the multifunctionality of phosphor materials, optical temperature sensors based on the thermal response of luminescence intensity ratio (LIR), lifetime, and bandwidth have attracted scientific attention due to their high accuracy, non-contact thermometry, and fast response.[21-26] Lifetime-based thermometers have gained popularity due to the low chances of erroneous temperature readout.[22] Recently, dual-wavelength emission materials have emerged as perfect candidates for ratiometric or lifetime-based temperature sensing, which utilize temperature-dependent energy transfer between the dopant ions and charge transfer (CT) between the host matrix and dopant ions.[27-29] Interestingly, the dual-wavelength emitting $Mn^{2+/4+}$-activated phosphors can be studied for ratiometric and lifetime thermometry based on the diverse temperature-dependent photoluminescence (PL) properties and thermal quenching (TQ) of $Mn^{2+/4+}$ ions.

Herein, we synthesized a series of $Mn^{2+/4+}$-activated Y_3Al_2-Ga_3O_{12} (YAGG) phosphors using solid-state synthesis reported in our earlier work,[3] which is detailed in the ESI.† We reported the stabilization of mixed valent states of Mn in the YAGG lattice and studied the photoluminescence properties of the dual-emitting $Y_3Al_2Ga_3O_{12}$:$Mn^{2+/4+}$ phosphor at different excitation energies, doping amounts and temperature. The luminescence and application prospects of the dual-emitting $Y_3Al_2Ga_3O_{12}$:$Mn^{2+/4+}$ phosphor have not been studied before to the best of our knowledge. The changes in the defects and oxidation state of Mn ions with composition were probed using positron annihilation lifetime spectroscopy (PALS) and electron paramagnetic resonance (EPR) spectroscopy. We investigated the temperature-dependent luminescence behaviour of $Mn^{2+/4+}$ ions in a wide temperature range of 10 K to 490 K. The evolution of the Mn^{2+} emission band with temperature is discussed in detail with respect to temperature-dependent CT and defect-induced self-reduction of $Mn^{4+} \rightarrow Mn^{2+}$. The excitation wavelength-dependent decay kinetics was studied as a function of temperature to understand the depopulation mechanism and charge transfer dynamics in $Mn^{2+/4+}$-activated YAGG system. We demonstrate that the dual-wavelength emitting YAGG:Mn phosphor (620 nm/675 nm) can be utilized for ratiometric and lifetime thermometry based on the diverse thermal response of luminescence and decay of $Mn^{2+/4+}$ ions. The characterization details are provided in the ESI† file (Section S1.2).

2. Results and discussion

2.1 Structural and morphological analysis

The XRD diffraction patterns of all the Mn-doped YAGG samples confirmed the phase purity and YAGG crystallized in a cubic system (*Ia3d* space group) (Fig. S1, ESI†). The garnet structure YAGG is composed of YO_8 dodecahedron, AlO_6/GaO_6 octahedron, and AlO_4/GaO_4 tetrahedron (Fig. S2, ESI†). Based on the ionic size, the Mn^{2+}/Mn^{4+} ions (0.67 Å/0.53 Å) preferably occupy the octahedral Al^{3+}/Ga^{3+} (0.535 Å/0.62 Å) sites to form Mn^{2+}/Mn^{4+} color centers.[27] The FTIR spectra show the characteristic bands of Ga–O and Al–O stretching frequencies in the 580–850 cm^{-1} region (Fig. S3, ESI†).[3] The TEM image of YAGG:0.02Mn shows that the sample crystallized as particles with irregular morphology and size ~ 1 μm (Fig. S4, ESI†). The EDS spectra confirmed the presence of Y, Al, Ga, Mn, and O elements in the YAGG:0.02Mn sample (Fig. S5, ESI†).

2.2 Photoluminescence study

The photoluminescence excitation (PLE) spectra show different profiles for 620 nm and 675 nm emissions (Fig. 1(a) and (b)). When excited at 280 nm, the emission spectra (Fig. 1(d)) show a broad red emission peaking at 620 nm along with weak sharp bands at 675 nm, which can be ascribed to the $^4T_1 \rightarrow {}^6A_1$ transition of Mn^{2+} ions and the $^2E \rightarrow {}^4A_2$ transition of Mn^{4+} ions located in the AlO_6/GaO_6 octahedra, respectively.[21,23] Mn^{2+} emission depends on the crystal field strength and red emission of Mn^{2+} ions in the YAGG lattice is in accordance with the octahedral coordination of Mn^{2+} ions.[6,30] Mn^{4+} ions with $3d^3$ electronic configuration occupy the octahedral sites due to the preferred octahedral coordination and size.[18,24] The absence of green emission of Mn^{2+} ions in the emission spectra negated the possible occupation of tetrahedral Al^{3+}/Ga^{3+} sites. This suggested the presence of $Mn^{2+/4+}$ ions in the YAGG:Mn samples, which was confirmed by EPR measurements. The presence of sextet EPR lines due to both $Mn^{2+/4+}$ ions are marked in the EPR spectra (Fig. S6 and S7, ESI†). To further confirm the presence of Mn^{2+} and Mn^{4+} ions and investigate the relative amounts of $Mn^{2+/4+}$ ions in the samples with different Mn doping contents, X-ray photoelectron spectroscopy (XPS) measurements were performed on two samples, *i.e.*, YAGG:0.02Mn and YAGG:0.06Mn. The XPS survey spectra of the two samples and Mn $2p_{3/2}$ spectra are presented in Fig. S8a–c (ESI†). The Mn $2p_{3/2}$ spectra for YAGG:0.02Mn and YAGG:0.06Mn can be deconvoluted into two peaks of Mn^{2+} at 640.9 eV and Mn^{4+} at 644.9 eV.[18,31] Though the peak positions remained similar, the relative peak areas of Mn^{2+} and Mn^{4+} show different order. In YAGG:0.02Mn, the area of the Mn^{2+} peak is much smaller than that of Mn^{4+}, while in the YAGG:0.06Mn sample, the area of the Mn^{2+} peak is relatively higher than that of YAGG:0.02Mn. This indicated that the Mn^{2+} concentration increased compared to Mn^{4+} with the increase in the doping amounts of Mn ions in the YAGG matrix, which can be explained by the self-reduction of Mn^{4+} ions to Mn^{2+} at higher doping concentrations, as discussed later.

The color tunability from the red emission of Mn^{2+} in YAGG:0.002Mn to the deep red emission of Mn^{4+} ions under different excitation wavelengths is depicted by the emission photographs captured by a camera (see inset of Fig. 1(d) and (e)). The emission spectra (λ_{ex} = 320 nm) show the typical sharp band emission of Mn^{4+} ions with less intense Mn^{2+} emission (Fig. 1(e)). Interestingly, upon excitation at 280 and 320 nm, which can be ascribed to $O^{2-} \rightarrow Mn^{2+}$ and $O^{2-} \rightarrow Mn^{4+}$ CT transitions, the dual-band emission bands of both Mn^{2+} and Mn^{4+} were observed in the PL emission spectra of the samples at 620 nm ($^4T_1 \rightarrow {}^6A_1$) and 675 nm ($^2E \rightarrow {}^4A_2$), respectively. Mn^{4+} emission dominates at λ_{ex} = 320 nm, and Mn^{2+} emission

19672 | *J. Mater. Chem. C*, 2024, **12**, 19671–19680

This journal is © The Royal Society of Chemistry 2024

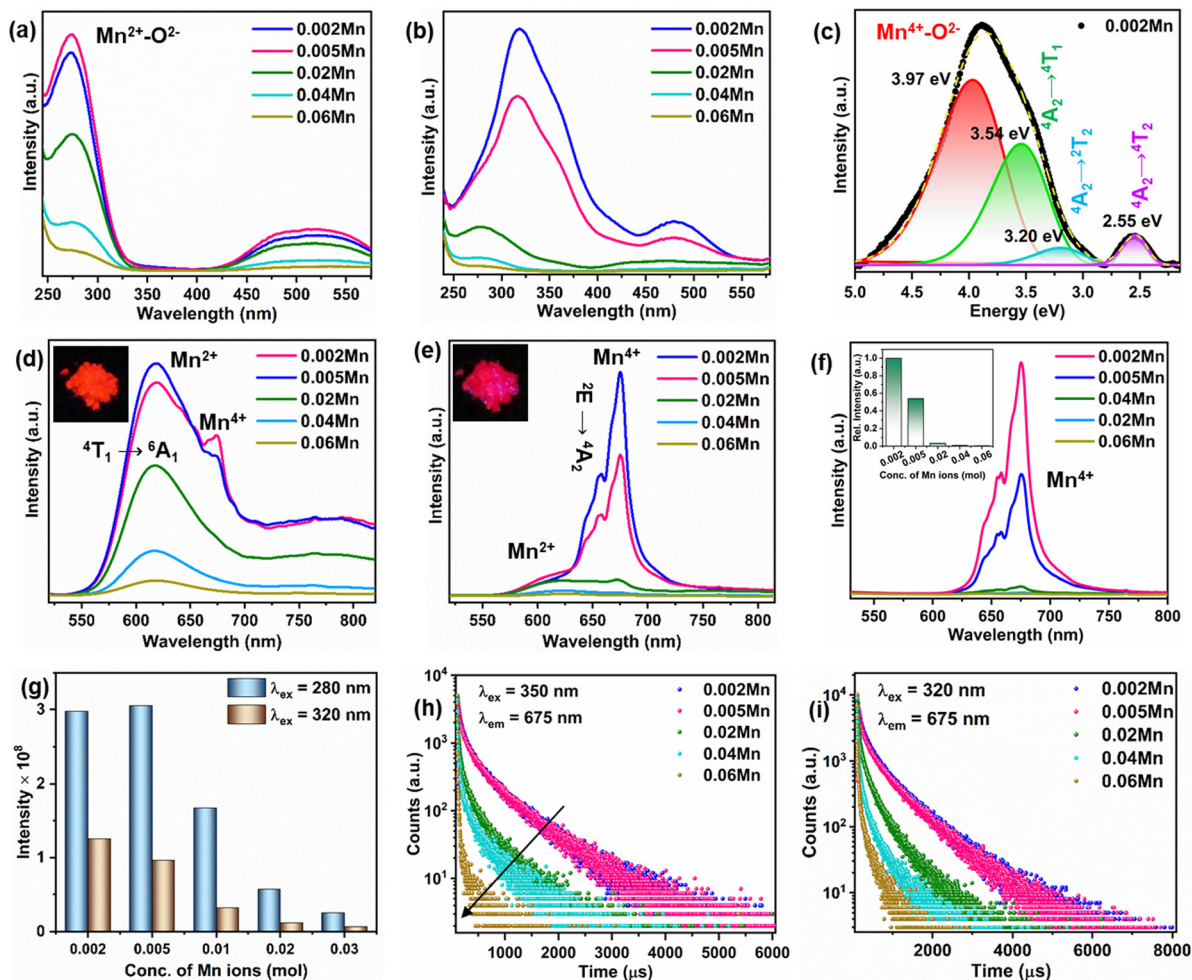**Fig. 1** PLE spectra of YAGG:xMn (x = 0.002–0.06 mol) phosphors monitored at (a) λ_{em} = 620 nm and (b) λ_{em} = 675 nm. (c) Deconvolution of the PLE spectrum of YAGG:0.002Mn monitored at 675 nm. PL emission spectra for (d) λ_{ex} = 280 nm and (e) λ_{ex} = 320 nm (emission photograph of YAGG:0.002Mn in inset). (f) PL emission spectra for λ_{ex} = 350 nm (inset showing the relative intensity with increasing Mn doping amounts). (g) Integral intensity as a function of Mn ions concentration. (h) Decay curves of Mn^{4+} ions at λ_{ex} = 350 nm and λ_{em} = 675 nm. (i) Decay curves of Mn ions at λ_{ex} = 320 nm and λ_{em} = 675 nm.

is more intense at λ_{ex} = 280 nm. The broad PLE spectrum (λ_{em} = 675 nm) of YAGG:0.002Mn is composed of four Gaussian bands centered at 312 nm (32 051 cm^{-1}), 350 nm (28 571 cm^{-1}), 388 nm (25 839 cm^{-1}) and 487 nm (20 533 cm^{-1}) due to the O^{2-} → Mn^{4+} CT, $^4A_2$ → $^4T_1$, $^4A_2$ → $^2T_2$ and $^4A_2$ → $^4T_2$ transitions of Mn^{4+} ions, respectively (Fig. 1(c)).[5] The PL emission spectra of the samples under 350 nm excitation, *i.e.*, the $^4A_2$ → $^4T_1$ transition of Mn^{4+} ions, showed single emission of Mn^{4+} ions at 675 nm only due to the ^2E → $^4A_2$ transition (Fig. 1(f)). The presence of dual-band emission and single-band emission under 320 and 350 nm excitations can be observed in Fig. S9 (ESI†). We evaluated the crystal field strength (D_q) and Racah parameter (B) of the Mn^{4+} sites in the YAGG:0.002Mn^{4+} sample using the following equations.

$$D_q/B = 15(x-8)/x^2 - 10x \qquad (1)$$

$$D_q = E(^4A_2 - {}^4T_2)/10 \qquad (2)$$

$$x = E(^4A_2 - {}^4T_1) - E(^4A_2 - {}^4T_2)/D_q \qquad (3)$$

The crystal field strength (D_q), Racah parameters (B), and crystal field strength (D_q/B) for Mn^{4+} were calculated as 2053 cm^{-1}, 798 cm^{-1}, and 2.57, respectively.

The variation of emission intensity as a function of Mn concentration is displayed in Fig. 1(f) and (g) where the optimal concentration is 0.002 mol and 0.005 mol for 320/350 nm and 280 nm excitation, respectively. The tuning of Mn emission color with doping amounts can be visualized from the CIE diagram (Fig. S10 and S11, ESI†). The excitation wavelength-dependent color tunability of Mn emission is achieved due to the different absorption efficiency of Mn$^{2+/4+}$ ions in the UV and near-UV regions (Fig. S12, ESI†). The concentration quenching resulted in the reduced emission intensity of both Mn$^{2+/4+}$ ions at higher Mn doping amounts.[32] The concentration quenching of both Mn$^{2+/4+}$ ions is caused by electric dipole–dipole interactions as θ = 5.76 and 6.36 (close to 6) were obtained from the log(I/x) *versus* log(x) plot shown in Fig. S13a and b (discussion in ESI†), respectively.[32]

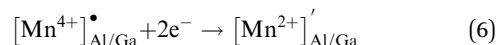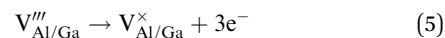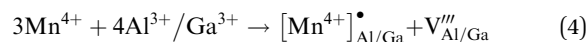With the increase in the Mn ions content, Mn^{4+} emission is quenched significantly and the broad emission of Mn^{2+} is

This journal is © The Royal Society of Chemistry 2024

J. Mater. Chem. C, 2024, **12**, 19671–19680 | **19673**

dominant in the YAGG samples with higher Mn content (Fig. S14 and S15, ESI†). This suggested the defect-induced self-reduction of $Mn^{4+} \rightarrow Mn^{2+}$ at higher Mn doping amounts.[33] Due to charge imbalance, the substitution of Al^{3+}/ Ga^{3+} sites by Mn^{4+} ions will induce the formation of cation vacancies ($V_{Al/Ga}$). The nature of defects with changing doping amount of Mn ions was probed using PALS technique (Fig. S16, ESI†). Typical positron annihilation lifetime spectra are shown in Fig. S16a (ESI†). All the lifetime spectra could be fitted as the sum of three exponentials or three positron annihilation lifetimes with longest lifetime of 1.5 to 2 ns with intensity $<0.5\%$. The typical fitting of the lifetime spectra is given as inset of Fig. S16a (ESI†). The long-lived component of $<0.5\%$ intensity is due to positronium formation on the surface of the powder particles. The other two positron lifetimes (τ_1 and τ_2), intensity of the second positron lifetime (I_2 and $I_1 \sim 100 - I_2$) and the intensity-weighted average positron lifetime (τ_{avg}) are given in Fig. S16b (ESI†).

The first positron lifetime (τ_1) is from the delocalised positron annihilation in the bulk of the sample while the second positron lifetime (τ_2) is from defects. The first positron lifetime in all the samples is in the range from 167 to 173 ps and is close to the lifetimes of 147–160 ps reported for the YAG samples in the literature.[34] With the doping of Mn, the first positron lifetime varied only marginally. A significant change is observed as a continuous reduction in the second positron lifetime, with the intensity of this component initially reducing and reaching a minimum at about 0.25–1% Mn doping and then increasing. Theoretical positron lifetimes for positron annihilations from various possible vacancies in YAG are reported.[35] As per the calculations, Y vacancies are expected to give positron lifetime of 341 ps, Al vacancy gives a lifetime of 275–279 ps, and oxygen vacancies about 238 ps. The second positron lifetime suggested that cation vacancies are formed initially at low Mn doping amount and finally lead to oxygen vacancies at higher Mn doping. Mn can be doped in variable oxidation states. It is expected that the doping of Mn^{4+} would lead to the formation of cation vacancies while Mn^{2+} would enhance the formation of oxygen vacancies for charge compensation. These results indicated that Mn might be doped as Mn^{4+} at lower concentrations while Mn^{2+} is favoured at higher concentrations. This result is in line with the XPS analysis; hence, it can be concluded that more Mn^{4+} ions get reduced to Mn^{2+} with the increase in the Mn doping amounts.

The presence of both Mn^{4+} and Mn^{2+} emission indicated abnormal self-reduction in the YAGG lattice. The charge compensation model has been used in earlier reports to explain the abnormal self-reduction from $Mn^{4+} \rightarrow Mn^{2+}$ ions.[15] The substitution of trivalent Al^{3+}/Ga^{3+} sites by tetravalent Mn^{4+} ions in YAGG will induce the formation of positively charged $\left[Mn^{4+}\right]^{\bullet}_{Al/Ga}$ and negatively charged $V'''_{Al/Ga}$ defects. To neutralize the excess positive charge, four Al^{3+}/Ga^{3+} ions will be replaced by three Mn^{4+} ions (eqn (1)). The generated $V'''_{Al/Ga}$ can act as electron donors, and the released electrons from the $V'''_{Al/Ga}$ defects can be captured by the electron acceptor

$\left[Mn^{4+}\right]^{\bullet}_{Al/Ga}$-defects. As a result, some of the Mn^{4+} ions are reduced to Mn^{2+}. The above processes can be explained by the following equations.

$$3Mn^{4+} + 4Al^{3+}/Ga^{3+} \rightarrow \left[Mn^{4+}\right]^{\bullet}_{Al/Ga} + V'''_{Al/Ga} \quad (4)$$

$$V'''_{Al/Ga} \rightarrow V^{\times}_{Al/Ga} + 3e^{-} \quad (5)$$

$$\left[Mn^{4+}\right]^{\bullet}_{Al/Ga} + 2e^{-} \rightarrow \left[Mn^{2+}\right]'_{Al/Ga} \quad (6)$$

In addition, the YAGG:0.02Mn samples were synthesized under air atmosphere using $MnCO_3$ and MnO_2 as raw Mn source. The PLE and emission spectra (Fig. S17, ESI†) show similar spectral profiles, which confirm the self-reduction of Mn^{4+} to Mn^{2+} ions in the YAGG matrix.

The luminescence decay profiles for the Mn-doped YAGG phosphors for emission at 675 nm and 620 nm (λ_{ex} = 320/ 350 nm and 280 nm) are presented in Fig. 1(h), (i) and Fig. S18 (ESI†), respectively. The average lifetimes (τ_{avg}) of Mn ions were calculated using a bi-exponential decay function.

$$I(t) = I_0 + A_1 e^{-t/\tau_1} + A_1 e^{-t/\tau_2} \quad (7)$$

where I_0 and $I(t)$ represent the emission intensities at zero offset and at 't' time, τ_1 and τ_2 are the two lifetime components, while A_1 and A_2 are constants, respectively. The lifetime values for the Mn-doped YAGG phosphors are summarized in Tables S1 and S2 (ESI†). The average lifetimes of the 675 nm emission (λ_{ex} = 320 nm) peak decreased from 652 µs to 276 µs on higher Mn doping (x = 0.002 to 0.06), which is consistent with the PL intensity trend due to non-radiative energy migration between Mn^{4+} ions.[36] Similarly, the lifetime value of Mn^{4+} ions decreased from 500 µs to 200 µs on higher Mn doping at λ_{ex} = 350 nm. The lifetime values of 620 nm emission (λ_{ex} = 280 nm) firstly increased from 354 µs to 360 µs and then decreased to 160 µs at higher Mn doping. Time-resolved emission spectroscopy (TRES) was performed for 280 nm excitation (Fig. S19, ESI†). With an increase in the delay times, both Mn^{2+} and Mn^{4+} emissions can be observed while only Mn^{2+} emissions are dominant at lower delay times.

2.3 Temperature-dependent PL study

Since the excitations at 280 and 320 nm fall in the excitation range of both Mn^{4+} and Mn^{2+} ions, the temperature-dependent luminescence behaviour of the dual-emission bands of $Mn^{2+/4+}$ ions can be investigated effectively using these two CT transitions. To understand the thermal behaviour of $Mn^{2+/4+}$ luminescence, the temperature-dependent PLE and emission spectra of $Mn^{2+/4+}$ under CT band excitation were recorded from 10 K to 490 K (Fig. 2(a)–(f)). The PLE spectra (λ_{em} = 620 nm) in Fig. 2(a) display an increase in the $O^{2-} \rightarrow Mn^{2+}$ CT band intensity initially up to 290 K, followed by decreased intensity at elevated temperatures (Fig. 3(a)). On the contrary, the PLE spectra (λ_{em} = 675 nm) shows a continuous decrease in the intensity of the $O^{2-} \rightarrow Mn^{4+}$ CT band with temperature (Fig. 3(a)). The temperature-dependent PL emission

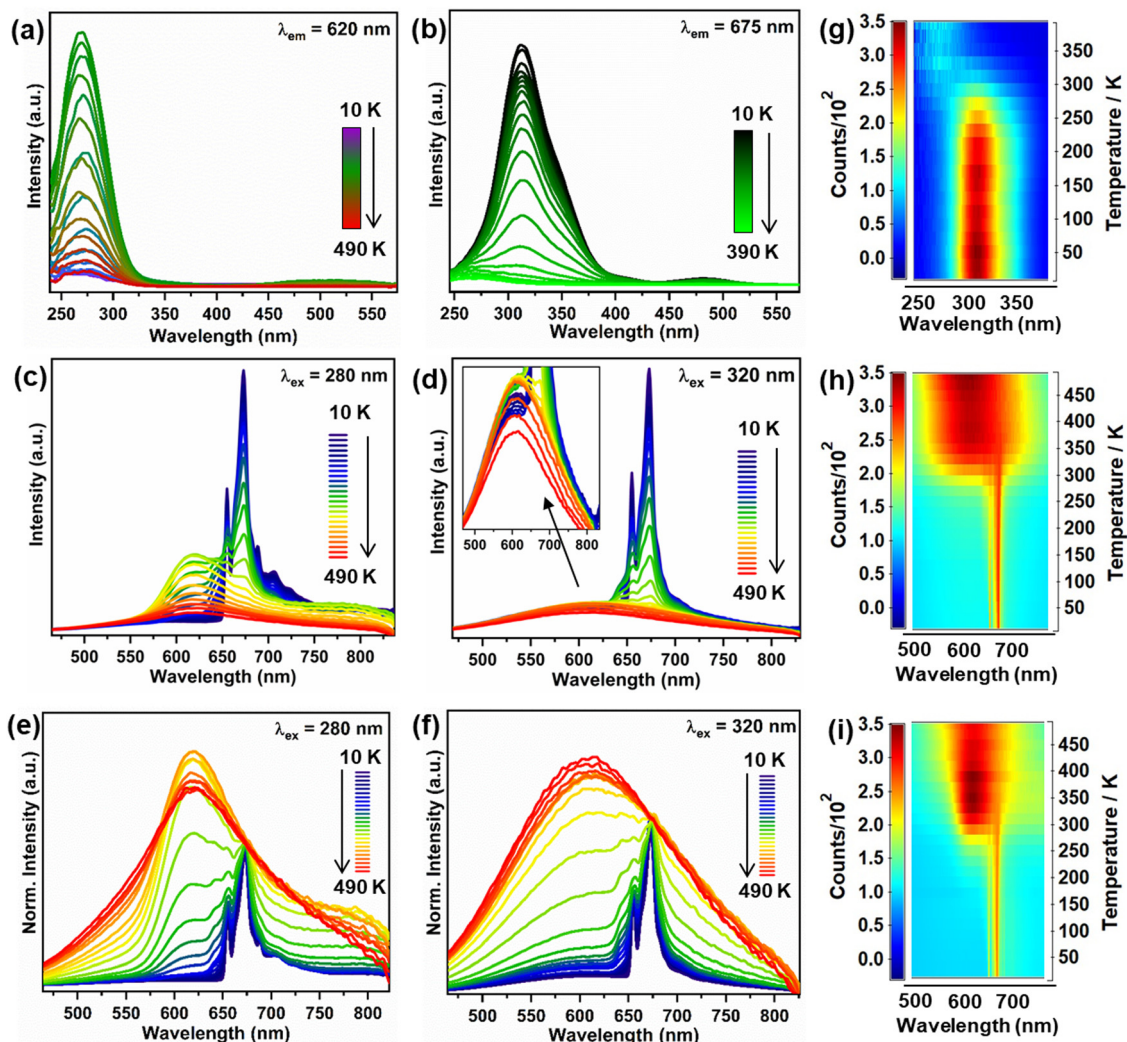**19674** | *J. Mater. Chem. C*, 2024, **12**, 19671–19680

This journal is © The Royal Society of Chemistry 2024

Fig. 2 Temperature-dependent PLE spectra of YAGG:0.002Mn in the range from 10 to 490 K at (a) λ_{em} = 620 nm and (b) λ_{em} = 675 nm. Temperature-dependent PL spectra at (c) λ_{ex} = 280 nm and (d) λ_{ex} = 320 nm (inset shows the zoomed-in emission spectra). Temperature-dependent normalized PL spectra at 675 nm under (e) λ_{ex} = 280 nm and (f) λ_{ex} = 320 nm. (g)–(i) Contour plots for the normalized intensity of the CT band (λ_{em} = 675 nm) and emission spectra (λ_{ex} = 320 and 280 nm), respectively.

spectra (λ_{ex} = 320 nm and 280 nm) demonstrated an abnormal trend in integral intensity change with temperature (Fig. 2(c) and (d)). The normalized emission spectra with respect to 675 nm emission shows that the spectral profile changes with temperature, where the Mn^{2+} emission becomes dominant at elevated temperatures (Fig. 2(e) and (f)). The broad emission at 620 nm (λ_{ex} = 280 nm) due to Mn^{2+} ions increased with temperature till 290 K and shows TQ above 310 K; however, Mn^{4+} emission at 675 nm undergoes continuous TQ (Fig. 2(g) and 3(a)). The above observations can be visualized from the contour plots (Fig. 2(g)–(i)). The TQ in the Mn^{4+} ions can be caused by the crossover of ^2E and $^4T_2$ parabolas (ΔE_1) or $^4T_2$ and $^4A_2$ parabolas (ΔE_2), which results in non-radiative relaxation.[37] The phonon-assisted crossover of $^4T_1$ and $^6A_1$ parabolas in the case of Mn^{2+} ions can result in non-radiative relaxation to the ground state (ΔE).[38]

The trend of total integral intensity under different excitation wavelengths is shown in Fig. S20 (ESI†). The trend of the

$O^{2-} \rightarrow Mn^{2+}$ CT band is similar to the 620 nm peak intensity variation with temperature. This indicated that the release of electrons from the traps with increasing temperature may strength the $O^{2-} \rightarrow Mn^{2+}$ CT, which led to the anti-TQ of Mn^{2+} emission (<290 K). The temperature dependence of the Mn^{2+} ion showing both anti-TQ and normal TQ can be fitted by the Shibata et al. model discussed in the ESI† (Fig. S21).[39] The values of activation energies for the anti-TQ of Mn^{2+} emission below 290 K is 686 cm^{-1}, normal TQ of Mn^{2+} emission after 310 K is 1955 cm^{-1}, and energy barrier for TQ of Mn^{4+} ions is 774 cm^{-1}. This suggested that the anti-TQ of Mn^{2+} ions and TQ of Mn^{4+} ions may be controlled by the thermal population of the $^4T_1$ state of Mn^{2+} ions and the simultaneous depopulation of the ^2E state of Mn^{4+} ions, respectively.

To get better insights into the depopulation and thermal quenching mechanisms, temperature-dependent decay curves were recorded at $Mn^{2+/4+}$ emission wavelengths in the temperature range from 10 K to 490 K. The lifetime values of Mn^{2+}

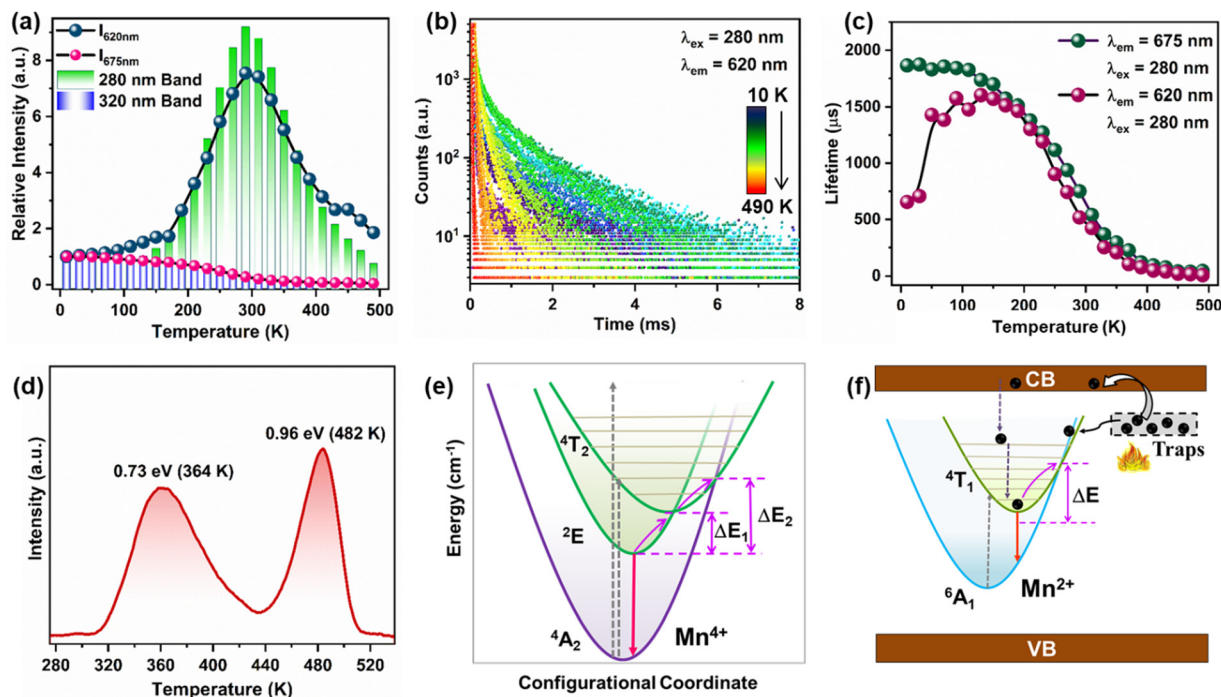This journal is © The Royal Society of Chemistry 2024

J. Mater. Chem. C, 2024, 12, 19671–19680 | 19675

Fig. 3 (a) Variation in the peak intensity at 620 nm and 675 nm with temperature (λ_{ex} = 280 nm) and the CT band intensity for λ_{em} = 620 nm and 675 nm. (b) Luminescence decay profiles as a function of temperature at λ_{ex} = 280 nm and λ_{em} = 620 nm. (c) Temperature variation of lifetime for λ_{ex} = 280 nm. (d) TL spectra of YAGG:0.02Mn when irradiated with 280 nm light. (e) Schematic illustration of radiative transitions and possible thermal quenching mechanisms for Mn^{4+} emission in octahedral coordination. (f) Schematic illustration of electron release from the traps and enhanced Mn^{2+} emission with the increase in temperature.

emission at 620 nm increases initially, which can be attributed to the thermal population of the $^4T_1$ state of Mn^{2+} ions, which modulates the PL intensity of Mn^{2+} emission (Fig. 3(b) and (c) and Fig. S22, S23, ESI†).[40] The lifetime increase indicated that with increasing temperature, the excited state population is increased by some thermally-activated processes. At higher temperature, the increased non-radiative pathways may result in the observed decrease in the lifetime values. In contrast, the lifetime values of 675 nm emission show a continuous decrease with temperature due to the increased non-radiative processes for the Mn^{4+} excited states (Fig. 3(c) and Fig. S22–S24, ESI†). The normal TQ of Mn^{4+} emission can be explained by the thermal cross-over of the excited states with the ground state of Mn^{4+} ions (Fig. 3(e)).

2.4 Mechanism of thermal quenching behaviour of $Mn^{2+/4+}$ ions

To investigate the nature of defects, the thermoluminescence (TL) spectrum for the YAGG:0.002$Mn^{2+/4+}$ was recorded sample upon irradiation with 280 nm light for 100 s. The TL spectra (Fig. 3(d)) shows two peaks at 364 K and 482 K, which can be attributed to the presence of V_O and $[Mn^{4+}]^\bullet_{Al/Ga}$ defects, respectively.[33] The trap depths of these defects were calculated as 0.73 eV and 0.96 eV, using the equation $E = T/500$ (eV). Fig. 3(f) shows the proposed mechanism for the anti-TQ of Mn^{2+} emission. The shallow traps can capture the electrons during UV excitation, which can be released to the conduction

band (CB) on increasing the temperature. The electrons in the CB can populate the excited $^4T_1$ state of Mn^{2+}. The increased thermal vibrations can also induce electron tunneling to the excited $^4T_1$ level of Mn^{2+} ions from the trap levels around the excited energy levels of Mn^{2+}. The above thermally-induced population of Mn^{2+} excited levels resulted in the enhancement of Mn^{2+} emission with temperature increase to 290 K. However, thermal quenching dominates at higher temperatures due to the thermal crossover of the $^4T_1$ and $^6A_1$ states. The observed trend can also be explained by the thermally-induced self-reduction of $Mn^{4+} \rightarrow Mn^{2+}$ ions as $V_{Ga/Al}$ can act as electron donors.[30,33] With the increase in temperature, the electrons are released from $V_{Ga/Al}$ and transferred to the nearby Mn^{4+} ions.[18]

2.5 Temperature sensing application

The diverse temperature-dependent behaviour of $Mn^{2+/4+}$ emission upon 280 nm excitation can be utilized for LIR-based ratiometric and lifetime thermometry. The LIR (620 nm/675 nm) (Fig. 4(a)) from 10 K to 330 K can be fitted with the following exponential equation.[41]

$$LIR_{(620/675)} = A + B\exp(-\Delta E/kT) \qquad (8)$$

Here, ΔE is the activation energy for thermal quenching, T is temperature (Kelvin), k is the Boltzmann constant, and A and B are constants. The absolute sensitivity (S_a) and relative sensitivity (S_r) values can be evaluated by the following

19676 | J. Mater. Chem. C, 2024, 12, 19671–19680
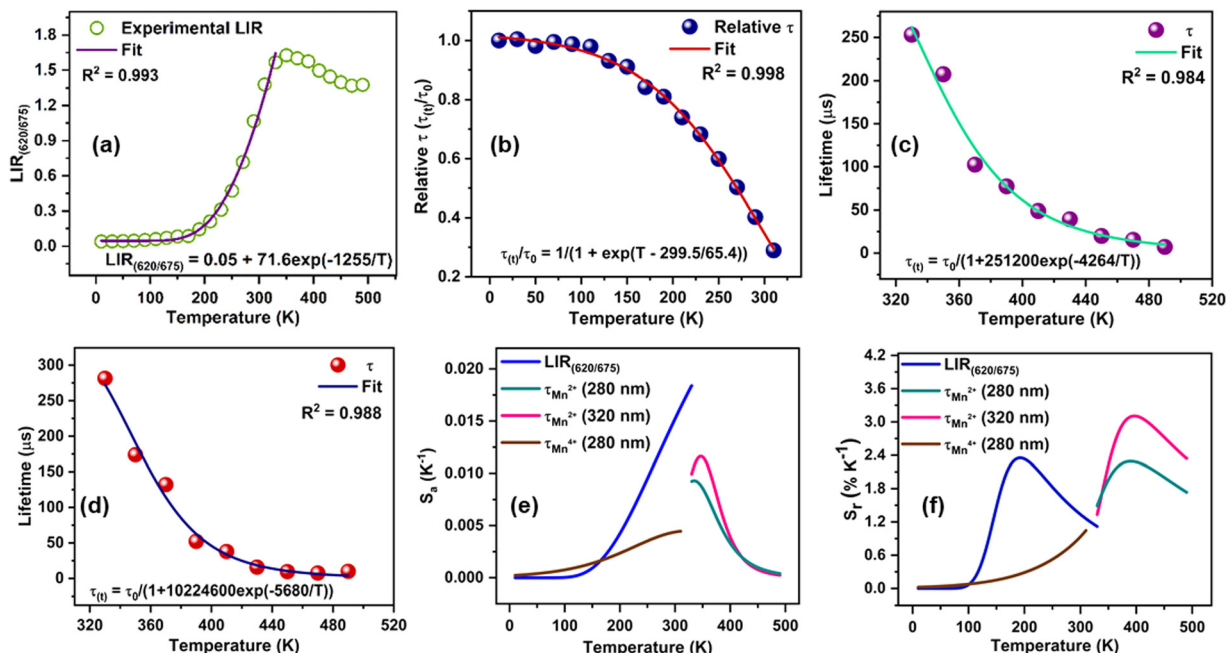
This journal is © The Royal Society of Chemistry 2024

Fig. 4 (a) Temperature dependence of LIR$_{(620/675)}$ and the fitting curve. Temperature dependence of relative τ values for (b) λ_{ex} = 280 nm and λ_{em} = 675 nm, (c) λ_{ex} = 280 nm and λ_{em} = 620 nm, (d) λ_{ex} = 320 nm and λ_{em} = 620 nm. (e) Corresponding S_a values as a function of temperature. (f) Corresponding S_r values as a function of temperature.

relations.

$$S_a \ (K^{-1}) = \left| \frac{dLIR}{dT} \right| \tag{9}$$

$$S_r \ (\% \ K^{-1}) = \frac{1}{LIR} \left| \frac{dLIR}{dT} \right| \times 100 \tag{10}$$

The S_a and S_r values as a function of temperature are shown in Fig. 4(e) and (f), respectively. The maximum S_a value of 0.018 K^{-1} (at 330 K) and high S_r of 2.35% K^{-1} (190 K) could be achieved for the Mn$^{2+/4+}$ LIR-based thermometer. An S_r value higher than 1.0% K^{-1} was retained up to 330 K. The temperature uncertainty (δT) can be evaluated using the following expression.

$$\delta T \ (K) = \frac{1}{S_r} \frac{\delta LIR}{LIR} \tag{11}$$

where $\delta LIR/LIR$ can be evaluated as the uncertainty of the measured LIR values.[40] The δT values in the range of 0.15–0.01 K were obtained for ratiometric thermometry.

The thermal dependence of the lifetime values of 675 nm emission under 280 nm excitation wavelength can be utilized for wide-range temperature sensing from 10 to 310 K. The sigmoidal temperature dependences of the relative lifetime ($\tau_{(t)}/\tau_0$) of Mn^{4+} ions can be fitted using the Boltzmann function as follows.

$$\Delta_\tau = \frac{\tau_{(t)}}{\tau_0} = \frac{1}{1 + A \exp(T - T_0/dT)} \tag{12}$$

where τ_0 and $\tau_{(t)}$ are the lifetime values at initial temperature T_0 and at 'T', respectively.

The temperature dependences of Mn^{2+} lifetime (λ_{ex} = 280 nm/320 nm) can be fitted in the temperature range from 330 K to 490 K using an equation derived from the Mott–Seitz model.[27]

$$\Delta_\tau = \tau_{(t)} = \frac{\tau_0}{1 + A \ \exp(-\Delta E/kT)} \tag{13}$$

where k is Boltzmann constant, and ΔE is the activation energy for non-radiative processes.

The S_a and S_r values for lifetime thermometry can be evaluated by the following relations.

$$S_a \ (K^{-1}) = \left| \frac{d\Delta_\tau}{dT} \right| \tag{14}$$

$$S_r \ (\% \ K^{-1}) = \frac{1}{\Delta_\tau} \left| \frac{d\Delta_\tau}{dT} \right| \times 100 \tag{15}$$

Lifetime thermometry based on the Boltzmann function using Mn^{4+} emission offers the maximum S_a value of 0.0045 K^{-1} (at 310 K), and S_r of 1.05% K^{-1} was attained at 310 K (Fig. 4(f)). Lifetime thermometry based on Mn^{2+} emission (λ_{ex} = 280 nm) displays the maximum S_a value of 0.009 K^{-1} (at 330 K) and S_r of 2.29% K^{-1} (390 K). Lifetime thermometry based on Mn^{2+} emission (λ_{ex} = 320 nm) displays the maximum S_a value of 0.012 K^{-1} (at 350 K) and S_r of 3.10% K^{-1} (390 K). The temperature uncertainty (δT) for lifetime thermometry can be

This journal is © The Royal Society of Chemistry 2024

J. Mater. Chem. C, 2024, 12, 19671–19680 | 19677

Table 1 Comparison of thermometric performance of our thermometer with similar reported thermometers

System	Type	Temp. range	S_r (% K^{-1})	Ref.
LaZnGa$_{11}$O$_{19}$(LZG):Cr^{3+}/Ni^{2+}	LIR	100–175 K, 200–475 K	2.4% K^{-1} at 475 K	42
Sr$_2$LuNbO$_6$:Mn^{4+}	LIR	12–523 K	0.55% K^{-1} at 136 K	43
	Lifetime	12–523 K	1.55% K^{-1} at 519 K	
SrGdLiTeO$_6$:Mn^{4+}/Eu^{3+}	Lifetime	300–600 K	0.229% K^{-1} at 573 K	44
Ca$_3$Ga$_2$Ge$_3$O$_{12}$:Mn^{3+}/Mn^{4+}	LIR	5–75 K	6% K^{-1} at 33 K	40
ZnGa$_{2-y}$Al$_y$O$_4$:Mn^{2+}/Mn^{4+}	LIR	100–475 K	4.345% K^{-1} at 350 K	17
Lu$_3$Al$_5$O$_{12}$:Ce^{3+}/Mn^{4+}	LIR	250–350 K	4.37% K^{-1} at 350 K	27
	Lifetime	250–350 K	3.22% K^{-1} at 350 K	
Mn^{4+}-doped BaLaCa$_{1-x}$Mg$_x$SbO$_6$	Lifetime	303–503 K	1.42% K^{-1} at 488 K	9
Y$_2$O$_3$:Ho^{3+}/Mg$_2$TiO$_4$:Mn^{4+}	LIR	RT–100 °C	4.6% °C^{-1} 0.9 at 473 K	45
	Lifetime	RT–100 °C		
Gd$_3$Al$_5$O$_{12}$:Mn^{3+}/Mn^{4+}	Lifetime	100–600 K	2.08% K^{-1} at 249 K	22
Y$_2$O$_3$:Yb^{3+}/Er^{3+}	Lifetime	298–338 K	0.50% K^{-1} at 310 K	46
Y$_3$Al$_2$Ga$_3$O$_{12}$:Mn^{2+}/Mn^{4+}	LIR	10–330 K	2.35% K^{-1} at 190 K	This work
	Lifetime (Mn^{4+})	10 to 310 K	1.05% K^{-1} at 310 K	
	Lifetime$_{280}$ (Mn^{2+})	330 to 490 K	2.29% K^{-1} at 390 K	
	Lifetime$_{320}$ (Mn^{2+})	330 to 490 K	3.10% K^{-1} at 390 K	

evaluated using the following expression

$$\delta T \ (K) = \frac{1}{S_r} \frac{\delta\tau}{\tau} \qquad (16)$$

where $\delta\tau/\tau$ can be evaluated as uncertainty in lifetime measurements, which was determined as 0.4% for repeated decay measurements. The δT values within 0.12–0.30 K indicated high resolution for temperature sensing in the range from 330 K to 490 K for lifetime thermometry using Mn^{2+} emission (Fig. S25, ESI†). Temperature sensing with high precision can be achieved in this work based on LIR and the lifetime of Mn$^{2+/4+}$ ions in the YAGG matrix.

The thermometric performance of our thermometer was compared with similar thermometers in Table 1. Hence, the lifetime thermometry displayed by the YAGG:Mn$^{2+/4+}$ phosphor is relatively higher than the earlier reported lifetime thermometers, and S_r greater than 1.0% K^{-1} can be achieved above 150 K. The reverse thermal response of Mn$^{2+/4+}$ ions can be utilized for temperature sensing at low temperatures. The lifetime of the two valence states can be used in different temperature ranges for temperature detection with high precision. Hence, the mixed valence state YAGG:Mn$^{2+/4+}$ phosphor is a potential candidate for a dual-mode temperature sensor. This work discussed the abnormal reverse thermal response of two ions, which can be utilized for targeted applications and provide useful insights into such mixed valent Mn$^{2+/4+}$ orange-red emitting phosphors.

3. Conclusion

In conclusion, YAGG:Mn$^{2+/4+}$ phosphors display different emission from red to deep red under different excitation wavelengths (280 and 320 nm). The luminescence tuning of orange-red emitting phosphors with doping concentration of Mn ions and excitation wavelength can be promising for designing orange-red emitting materials. The Mn^{2+}/Mn^{4+} ions display distinctive luminescence and decay time behaviour, which can be utilized for potential wide range optical thermometry with high temperature

sensitivity. The ratiometric thermometer offers a high maximum S_r value of 2.35% K^{-1} (190 K). Lifetime thermometry at two different excitation wavelengths, namely, 280 nm and 320 nm, presents temperature read-out with a high maximum S_r value of 3.10% K^{-1} (390 K) and 1.05% K^{-1} (310 K), respectively. This work reports a single metal (two oxidation states)-based dual emitting ratiometric and lifetime thermometer with wide sensing range. Additionally, this work demonstrated the self-reduction of Mn ions in Mn-doped garnet materials and abnormal temperature-dependent luminescence properties of Mn$^{2+/4+}$ ions.

Data availability

The data supporting this article have been included as part of the ESI.†

Conflicts of interest

There are no conflicts of interests to declare.

Acknowledgements

References

1 A. Balhara, S. K. Gupta, M. Abraham, B. Modak, S. Das, C. Nayak, H. V. Annadata and M. Tyagi, Trap engineering through chemical doping for ultralong X-ray persistent luminescence and anti-thermal quenching in Zn$_2$GeO$_4$, *J. Mater. Chem. C*, 2024, **12**(5), 1728–1745.

2 A. Balhara, S. K. Gupta, M. Abraham, A. K. Yadav, M. Jafar and S. Das, Negative thermal expansion in Sc2Mo3O12:

19678 | *J. Mater. Chem. C*, 2024, **12**, 19671–19680

This journal is © The Royal Society of Chemistry 2024

Sm3+ for white LEDs and unveiling the impact of phase transition on cryogenic luminescence, *J. Mater. Chem. C*, 2024, **12**(31), 11955–11966.

3 A. Balhara, S. K. Gupta, B. Modak, M. Abraham, A. K. Yadav, H. V. Annadata, S. Das, N. S. Rawat and K. Sudarshan, Synergy between structural rigidity and cluster defects in a bright near-infrared Cr3+-based phosphor for excellent thermal stability and long afterglow, *J. Mater. Chem. C*, 2024, **12**(26), 9716–9732.

4 S. K. Gupta, B. Modak, M. Abraham, S. Das, R. Gupta, K. G. Girija, M. Mohapatra and K. Sudarshan, Defect induced tunable light emitting diodes of compositionally modulated zinc gallium germanium oxides, *Chem. Eng. J.*, 2023, **474**, 145595.

5 K. Li and R. Van Deun, Realizing a novel dazzling far-red-emitting phosphor NaLaCaTeO6:Mn4+ with high quantum yield and luminescence thermal stability via the ionic couple substitution of Na+ + La3+ for 2Ca2+ in Ca3TeO6:Mn4+ for indoor plant cultivation LEDs, *Chem. Commun.*, 2019, **55**(72), 10697–10700.

6 Q. Zhou, L. Dolgov, A. M. Srivastava, L. Zhou, Z. Wang, J. Shi, M. D. Dramićanin, M. G. Brik and M. Wu, Mn2+ and Mn^{4+} red phosphors: synthesis, luminescence and applications in WLEDs. A review, *J. Mater. Chem. C*, 2018, **6**(11), 2652–2671.

7 S. Adachi, Mn^{4+} *vs.* Mn^{2+}—A comparative study as efficient activator ions in phosphor materials: A review, *J. Lumin.*, 2023, 119993.

8 K. Chen, Z. Shao, C. Zhang, S. Jia, T. Deng, R. Zhou, Y. Zhou and E. Song, Illuminating the path to high-precision dual-mode optical thermometry: A Mn4+-activated oxyfluoride single crystal for a portable optical fiber thermometric platform, *Chem. Eng. J.*, 2023, **477**, 147165.

9 G. Li, G. Li, Q. Mao, L. Pei, H. Yu, M. Liu, L. Chu and J. Zhong, Efficient luminescence lifetime thermometry with enhancedMn^{4+}-activated BaLaCa$_{1-x}$Mg$_x$SbO$_6$ red phosphors, *Chem. Eng. J.*, 2022, **430**, 132923.

10 C. Lu and W. You, Harnessing solid-state ion exchange for the environmentally benign synthesis of high-efficiency Mn4+-doped phosphors, *Chem. Commun.*, 2024, **60**(41), 5399–5402.

11 Z. Zhou, N. Zhou, M. Xia, M. Yokoyama and H. B. Hintzen, Research progress and application prospects of transition metal Mn4+-activated luminescent materials, *J. Mater. Chem. C*, 2016, **4**(39), 9143–9161.

12 F. Fang, Y. Jin, H. Chen, H. Lin, Y. Li, Y. Xiong, F. Meng, L. Cao, F. Huang and L. Ma, Multiple encrypted dynamic fluorescent anti-counterfeiting and optical temperature detection of Ca2Ge7O16:Cr3+,Mn2+, *J. Lumin.*, 2024, **269**, 120514.

13 F. Fang, Y. Jin, W. Hu, Y. Chen, Y. Wei, Z. Zhang, C. Wang, F. Meng, L. Cao and F. Huang, Optical Information Transmission and Multimode Fluorescence Anticounterfeiting of Ca$_{2-x}$Mg$_x$Ge$_7$O$_{16}$:Mn2+, *Inorg. Chem.*, 2024, **63**(15), 6938–6947.

14 L. Dong, L. Zhang, Y. Jia, B. Shao, W. Lü, S. Zhao and H. You, Enhancing Luminescence and Controlling the Mn Valence State of Gd$_3$Ga$_{5-x-\delta}$Al$_{x-y+\delta}$O$_{12}$:yMn Phosphors by the Design of the Garnet Structure, *ACS Appl. Mater. Interfaces*, 2020, **12**(6), 7334–7344.

15 L. Dong, L. Zhang, Y. Jia, B. Shao, W. Lü, S. Zhao and H. You, Site occupation and luminescence of novel orange-red Ca$_3$M$_2$Ge$_3$O$_{12}$:Mn2+,Mn4+ (M = Al, Ga) phosphors, *ACS Sustainable Chem. Eng.*, 2020, **8**(8), 3357–3366.

16 G. Doke, G. Krieke, A. Antuzevics, A. Sarakovskis and B. Berzina, Optical properties of red-emitting long afterglow phosphor Mg2Si1$_x$GexO4:Mn2+/Mn4+, *Opt. Mater.*, 2023, **137**, 113500.

17 L. Dong, L. Zhang, Y. Jia, Y. Xu, S. Yin and H. You, ZnGa2–yAlyO4:Mn2+,Mn4+ Thermochromic Phosphors: Valence State Control and Optical Temperature Sensing, *Inorg. Chem.*, 2020, **59**(21), 15969–15976.

18 L. Zheng, L. Zhang, L. Fang, H. Wu, H. Wu, G.-H. Pan, Y. Yang, Y. Luo, Z. Hao and J. Zhang, Be2+-Induced Red Emission Enhancement in CaAl12O19:Mn4+ for Wide Color Gamut Display: Suppressing Self-Reduction of Mn4+ to Mn2+, *Adv. Opt. Mater.*, 2024, **12**(3), 2301480.

19 D. Guo, Z. Wang, N. Wang, B. Zhao, Z. Li, J. Chang, P. Zhao, Y. Wang, X. Ma, P. Li and H. Suo, Doping-mediated thermal control of phase transition for supersensitive ratiometric luminescence thermometry, *Chem. Eng. J.*, 2024, **492**, 152312.

20 X. Zhang, Y. Xu, X. Wu, S. Yin, C. Zhong, C. Wang, L. Zhou and H. You, Optical thermometry and multi-mode anti-counterfeiting based on Bi3+/Ln3+ and Ln3+ doped Ca2ScSbO6 phosphors, *Chem. Eng. J.*, 2024, **481**, 148717.

21 W. Liu, D. Zhao, R.-J. Zhang, Q.-X. Yao and S.-Y. Zhu, Fluorescence lifetime-based luminescent thermometry material with lifetime varying over a factor of 50, *Inorg. Chem.*, 2022, **61**(41), 16468–16476.

22 L. Marciniak and K. Trejgis, Luminescence lifetime thermometry with Mn3+–Mn4+ co-doped nanocrystals, *J. Mater. Chem. C*, 2018, **6**(26), 7092–7100.

23 E. Song, M. Chen, Z. Chen, Y. Zhou, W. Zhou, H.-T. Sun, X. Yang, J. Gan, S. Ye and Q. Zhang, Mn2+-activated dual-wavelength emitting materials toward wearable optical fibre temperature sensor, *Nat. Commun.*, 2022, **13**(1), 2166.

24 M. Szymczak, W. Piotrowski, P. Woźny, M. Runowski and L. Marciniak, A highly sensitive lifetime-based luminescent manometer and bi-functional pressure–temperature sensor based on a spectral shift of the R-line of Mn4+ in K2Ge4O9, *J. Mater. Chem. C*, 2024, **12**(19), 6793–6804.

25 H. Zhang, J. Yao, K. Zhou, Y. Yang and H. Fu, Thermally activated charge transfer in dual-emission Mn2+-alloyed perovskite quantum wells for luminescent thermometers, *Chem. Mater.*, 2022, **34**(4), 1854–1861.

26 K. Li, Z. Zhang, D. Zhu and C. Yue, Excellent temperature sensitivities based on the FIR technique of up-conversion luminescence in a novel NaLaTi$_2$O$_6$:Yb3+,Tm3+ material, *Inorg. Chem. Front.*, 2024, **11**, 7464–7474.

27 Y. Chen, J. He, X. Zhang, M. Rong, Z. Xia, J. Wang and Z.-Q. Liu, Dual-mode optical thermometry design in Lu3Al5O12:Ce3+/Mn4+ phosphor, *Inorg. Chem.*, 2020, **59**(2), 1383–1392.

This journal is © The Royal Society of Chemistry 2024

J. Mater. Chem. C, 2024, **12**, 19671–19680 | **19679**

28 F. Jahanbazi and Y. Mao, Recent advances on metal oxide-based luminescence thermometry, *J. Mater. Chem. C*, 2021, **9**(46), 16410–16439.

29 W. Piotrowski, K. Trejgis, K. Maciejewska, K. Ledwa, B. Fond and L. Marciniak, Thermochromic luminescent nanomaterials based on Mn4+/Tb3+ codoping for temperature imaging with digital cameras, *ACS Appl. Mater. Interfaces*, 2020, **12**(39), 44039–44048.

30 Y. Xiao, P. Xiong, S. Zhang, Y. Sun, N. Yan, Z. Wang, Q. Chen, P. Shao, M. G. Brik and S. Ye, Cation-defect-induced self-reduction towards efficient mechanoluminescence in Mn2+-activated perovskites, *Mater. Horiz.*, 2023, **10**(9), 3476–3487.

31 Y. Chen, J. Chen, J. Liang, J. He, Z.-Q. Liu and Y. Yin, Localized Charge Accumulation Driven by Li+ Incorporation for Efficient LED Phosphors with Tunable Photoluminescence, *Chem. Mater.*, 2020, **32**(22), 9551–9559.

32 M. Zhang, A. Sun, X. Li, S. Sun, W. Ding, D. Fang, B. Mi and Z. Q. Gao, Unveiling luminescence property of Li2MgGeO4:Mn4+ featuring tetrahedral crystallographic-site occupancy of Mn4+, *Dalton Trans.*, 2024, **53**, 10168–10177.

33 P. Zhang, Z. Zheng, L. Wu, Y. Kong, Y. Zhang and J. Xu, Self-reduction-related defects, long afterglow, and mechanoluminescence in centrosymmetric Li2ZnGeO4:Mn2+, *Inorg. Chem.*, 2021, **60**(23), 18432–18441.

34 F. Selim, C. Varney, M. Tarun, M. Rowe, G. Collins and M. McCluskey, Positron lifetime measurements of hydrogen passivation of cation vacancies in yttrium aluminum oxide garnets, *Phys. Rev. B: Condens. Matter Mater. Phys.*, 2013, **88**(17), 174102.

35 A. Marinopoulos, First-principles study of the formation energies and positron lifetimes of vacancies in the Yttrium-Aluminum Garnet Y3Al5O12, *Eur. Phys. J. B*, 2019, **92**, 1–9.

36 D. Chen, Y. Zhou, W. Xu, J. Zhong, Z. Ji and W. Xiang, Enhanced luminescence of Mn4+:Y3Al5O12 red phosphor via impurity doping, *J. Mater. Chem. C*, 2016, **4**(8), 1704–1712.

37 T. Senden, R. J. A. van Dijk-Moes and A. Meijerink, Quenching of the red Mn4+ luminescence in Mn4+-doped fluoride LED phosphors, *Light: Sci. Appl.*, 2018, **7**(1), 8.

38 A. J. van Bunningen, A. D. Sontakke, R. van der Vliet, V. G. Spit and A. Meijerink, Luminescence Temperature Quenching in Mn2+ Phosphors, *Adv. Opt. Mater.*, 2023, **11**(6), 2202794.

39 H. Shibata, Negative Thermal Quenching Curves in Photoluminescence of Solids, *Jpn. J. Appl. Phys.*, 1998, **37**(2R), 550.

40 Y. Wang, D. Włodarczyk, M. G. Brik, J. Barzowska, A. Shekhovtsov, K. Belikov, W. Paszkowicz, L. Li, X. Zhou and A. Suchocki, Effect of temperature and high pressure on luminescence properties of Mn3+ ions in Ca3Ga2Ge3O12 single crystals, *J. Phys. Chem. C*, 2021, **125**(9), 5146–5157.

41 Z. Cheng, J. Huang, G. Lu, Y. Wu, M. Avdeev, T. Yang and P. Jiang, Mg4InSbO8 Spinel: Double 2:1 Ordering in Tetrahedral and Octahedral Sublattices and Perspective Application as an Optical Thermometer *via* Mn2+/4+ Doping, *Chem. Mater.*, 2023, **35**(22), 9669–9681.

42 Q. Zhang, G. Li, G. Li, D. Liu, P. Dang, L. Qiu, H. Lian, M. S. Molokeev and J. Lin, Optical Thermometer Based on Efficient Near-Infrared Dual-Emission of Cr3+ and Ni2+ in Magnetoplumbite Structure, *Adv. Opt. Mater.*, 2024, **12**(1), 2301429.

43 Z. Chen, S. Du, K. Zhu, Z. Tian, J. Zhang, F. Li, S. Zhang, S. Zhao, W. Cui and X. Yuan, Mn4+-activated double-perovskite-type Sr2LuNbO6 multifunctional phosphor for optical probing and lighting, *ACS Appl. Mater. Interfaces*, 2023, **15**(23), 28193–28203.

44 L. Li, G. Tian, Y. Deng, Y. Wang, Z. Cao, F. Ling, Y. Li, S. Jiang, G. Xiang and X. Zhou, Constructing ultra-sensitive dual-mode optical thermometers: Utilizing FIR of Mn4+/Eu3+ and lifetime of Mn4+ based on double perovskite tellurite phosphor, *Opt. Express*, 2020, **28**(22), 33747–33757.

45 M. Sekulić, V. Đorđević, Z. Ristić, M. Medić and M. D. Dramićanin, Highly sensitive dual self-referencing temperature readout from the Mn4+/Ho3+ binary luminescence thermometry probe, *Adv. Opt. Mater.*, 2018, **6**(17), 1800552.

46 L. F. dos Santos, J. A. Galindo, K. D. O. Lima, A. R. Pessoa, A. M. Amaral, L. D. S. Menezes and R. R. Gonçalves, Lifetime-based luminescence thermometry from Yb3+/Er3+ codoped nanoparticles suspended in water, *J. Lumin.*, 2023, **262**, 119946.